COMMUNICATION

Chemically synthesized poly(3,4-ethylenedioxythiophene) conducting polymer as a robust electrocatalyst for highly efficient dye-sensitized solar cells†

Masud, [ID] [a,b,c] Md. Aftabuzzaman, [ID] [a] Haoran Zhou,[a,d] Saehyun Kim,[b] Jaekyung Yi,[e] Sarah S. Park, [ID] [e] Youn Soo Kim [ID] *[b] and Hwan Kyu Kim [ID] *[a]

Chemically synthesized PEDOT (poly(3,4-ethylenedioxythiophene)) nanomaterials, with various nanostructured morphologies as well as different intrinsic electrical conductivities and crystallinities, were compared as electrocatalysts for Co(ɪɪɪ) reduction in dye-sensitized solar cells (DSSCs). Electrochemical parameters, charge transfer resistance toward the electrode/electrolyte interface, catalytic activity for Co(ɪɪɪ)-reduction, and diffusion of cobalt redox species greatly depend on the morphology, crystallinity, and intrinsic electrical conductivity of the chemically synthesized PEDOTs and optimization of the fabrication procedure for counter electrodes. The PEDOT counter electrode, fabricated by spin coating a DMSO-dispersed PEDOT solution with an ordered 1D structure and nanosized fibers averaging 70 nm in diameter and an electrical conductivity of ~16 S cm^{-1}, exhibits the lowest charge transfer resistance, highest diffusion for a cobalt redox mediator and superior electrocatalytic performance compared to a traditional Pt-counter electrode. The photovoltaic performance of the DSSC using chemically synthesized PEDOT exceeds that of a Pt-electrode device because of the enhanced current density, which is directly related to the superior electrocatalytic ability of PEDOT for Co(ɪɪɪ)-reduction. This simple spin-coated counter electrode prepared using cheap and scalable chemically synthesized PEDOT can be a potential alternative to the expensive Pt-counter electrode for cobalt and other redox electrolytes in DSSCs and various flexible electronic devices.

aGlobal GET-Future Lab., Department of Advanced Materials Chemistry, Korea University, 2511 Sejong-ro, Sejong 339-700, Republic of Korea.
E-mail: hkk777@korea.ac.kr
bDepartment of Materials Science and Engineering, Pohang University of Science and Technology (POSTECH), 77 Cheongam-Ro, Nam-Gu Pohang, Gyeongbuk, Republic of Korea. E-mail: ysookim@postech.ac.kr
cDepartment of Biomedical Engineering, College of Life Science and Biotechnology, Dongguk University, Seoul 04620, Republic of Korea
dRenewable Energy Materials Laboratory (REML), Advanced Institute of Convergence Technology, Seoul National University, Suwon 16229, Republic of Korea
eDepartment of Chemistry, Pohang University of Science and Technology (POSTECH), Pohang 37673, Republic of Korea
†Electronic supplementary information (ESI) available. See DOI: https://doi.org/10.1039/d4nr00949e

1. Introduction

Conducting polymers (CPs) possess delocalized conjugated structures, which are widely studied and applied as electrocatalysts and photocatalysts in various energy-related devices, sensors, and environmental remediation because of their excellent catalytic ability, tunable electrical conductivities, and unique electrochemical and optical properties.[1–5] Dye-sensitized solar cells (DSSCs) are emerging photovoltaics, which mimic natural photosynthesis to convert light to electricity. The essential requirements of an electrocatalyst for DSSCs are high electrical conductivity, large surface area, and low charge transfer resistance in the electrode/electrolyte interface. A conducting polymer can fulfill all requirements to be an efficient counter electrode for DSSCs. Generally, platinum is widely used as an electrocatalyst in DSSCs because of its high catalytic ability and low charge transfer resistance, especially for iodine electrolytes. However, some drawbacks of Pt-counter electrodes include high cost; low abundance; instability toward iodine electrolytes; reaction with iodine electrolytes and PtI_4 formation, especially by a vapor deposited Pt thin layer;[6] less effectiveness toward metal-complexes and organic redox mediators[7] have encouraged researchers to find alternative efficient counter electrode catalysts for DSSCs. Because of the limitation of open circuit voltage (V_{oc}), high volatility, and corrosion of the Ag grid due to iodine electrolytes, metal complexes such as Co complexes and Cu complexes are promising redox electrolytes to enhance V_{oc} and overall efficiency of the device.[8] The significant power conversion efficiency, about 14–15%, for DSSCs has been reported using cobalt and copper complex redox electrolytes.[9–11] Therefore, the demand for alternative Pt-free counter electrodes, especially for cobalt and copper electrolytes, is very prominent, and a conducting polymer appears as a suitable candidate. Among

the conducting polymers, polypyrrole,[12,13] polyaniline,[14] poly (3,4-ethylenedioxythiophene) (PEDOT), and their derivatives[1,11,15–17] have been applied as electrocatalysts in DSSCs owing to their low cost and large-scale production, structural variation with nanoscale morphologies, tunable electrical conductivity, high chemical stability and low toxicity.

Among the various conducting polymers, PEDOT can be a promising electrocatalyst material because of its high conductivity, excellent chemical and physical stability under ambient conditions, optical transparency in the visible range, and easy doping and synthesis.[18,19] PEDOT can be synthesized by chemical oxidative polymerization or the electrodeposition process. Both processes follow the same oxidative mechanism. In electrodeposition, PEDOT is doped by the counteranion of electrolytes used for the electrochemical process, while in chemical synthesis, PEDOT is doped by the counteranion of the oxidant. The electrochemical synthesis limits the reaction on the surface of the conducting electrode substrate, and nanostructured PEDOT deposits on the substrate as a film. On the other hand, chemically synthesized PEDOTs are powdery nanomaterials and can be easily scaled up.[20]

The remarkable advancement for DSSC has been obtained using the PEDOT conducting polymer-based counter electrodes.[1,15] In most cases, PEDOTs are electrodeposited on the fluorine-doped tin oxide (FTO) coated glass substrate to fabricate efficient counter electrodes for cobalt and copper electrolytes.[1,15] However, for large-scale production and application in flexible devices, chemical oxidative synthesis can be a better option. The performance of the chemically synthesized PEDOT as an electrocatalyst depends on the nanostructural morphology, conductivity, crystallinity, chemical and thermal stability; these can be varied on the synthetic conditions, *e.g.*, concentration and type of oxidant, counter anion of the oxidant, temperature, surfactants, and reaction medium. Therefore, depending on the application, an effective synthetic procedure of PEDOT is required. There are few reports about chemically synthesized PEDOT for the application as an electrocatalyst counter electrode in DSSCs and, in most cases, with iodine electrolytes.[21,22] Their reported synthetic conditions were also somewhat different in terms of temperature and surfactant concentration applied here, which can affect the morphology and electrical properties of the nanomaterials.[21,22]

In this study, four different types of PEDOT nanomaterials were synthesized by aqueous chemical oxidative polymerization at room temperature by varying oxidants, the concentration of oxidant, and the presence or absence of surfactant to obtain PEDOTs with different nanostructural morphology, intrinsic electrical conductivity, and crystallinity. The counter electrode was developed by spin-coating the dispersed PEDOT solution in a dimethyl sulfoxide (DMSO) solvent without using any binder and drying in a vacuum oven at 70 °C. The green solvent DMSO was chosen because it can effectively disperse the synthesized nanoparticles while maintaining their as-synthesized nanostructure morphology, as confirmed through high-resolution scanning electron microscopy (SEM) imaging. Here, the developed simple procedure for the counter elec-

trode by chemically synthesized PEDOT can be comparable, even superior, to drop-casted Pt-counter electrode and can be an alternative for cobalt redox electrolytes and other redox electrolyte systems.

2. Results and discussion

2.1 Chemically synthesized PEDOT nanomaterials

2.1.1 Synthetic conditions and chemical characterization of PEDOT nanomaterials. PEDOT nanomaterials were synthesized by aqueous oxidative polymerization of 3,4-ethylenedioxythiophene (EDOT) using ammonium persulfate (APS) or iron(III) chloride oxidant with or without sodium dodecyl sulfonate (SDS) surfactant at room temperature (see Fig. 1a).[23,24] PEDOT-1 and PEDOT-2 were synthesized using the APS oxidant without a surfactant under the same reaction conditions except for the concentration of APS; the APS concentration was doubled for PEDOT-2 synthesis. PEDOT-3 was synthesized in the presence of 2.5 mM SDS surfactant using the same APS concentration as PEDOT-2 synthesis. PEDOT-4 was synthesized in the presence of 2.5 mM SDS surfactant using $FeCl_3$ oxidant.

The chemically synthesized PEDOTs were characterized by elemental analysis (see Table S1†), FT-IR (see Fig. 1b),[25,26] UV-vis-NIR absorption spectroscopy (see Fig. 1c), and energy dispersive X-ray spectroscopy (EDS) elemental mapping (see Fig. S1†). The PEDOT obtained by APS oxidative polymerization is most probably doped by available sulfate ions produced in the reaction.[27,28] The $\nu 3$ band of the sulfate around ~1090 cm^{-1} can be overlapped with the PEDOT band in the IR spectrum.[28] The doping level of sulfate in the APS synthesized PEDOTs can be estimated from elemental analysis from the consideration of all elemental carbon coming from PEDOT and sulfur coming from either thiophane ring in PEDOT or sulfate dopant according to the procedure of Chiu et al. (see Table S1†).[28] The EDS elemental mapping shows the distribution of carbon, sulfur, oxygen, and chloride in chemically synthesized PEDOT nanomaterials (see Fig. S1†). In the FT-IR spectrum (see Fig. 1b), the peaks at 1337 and 1514 cm^{-1} correspond to the C–C or C=C stretching frequencies of the quinoid structure and ring stretching of the thiophene ring.[26,29] The stretching of the alkylenedioxy groups corresponds to the vibration at 1200, 1141, and 1087 cm^{-1}.[26] The peaks at 982, 842, and 689 cm^{-1} correspond to the C–S bond stretching in the thiophene ring.[26,29] The existence of the vibration band around 1640 cm^{-1} was related to the doping level of the chemically synthesized PEDOTs, which is probably due to the C=C bond according to the report of Fichet et al.[30,31] All chemically synthesized PEDOTs, dispersed in DMSO, show characteristic absorption peaks at 400–700 nm due to π–π* transitions along the polymer chain (see UV-vis-NIR absorption spectra in Fig. 1c).[31–33] The oxidized state of PEDOT (polaron/bipolaron) can be attributed to the broad absorption band at 750–1050 nm, maxima ~880 nm, (see Fig. 1c).[31,33] The estimation of the exact molecular weight of
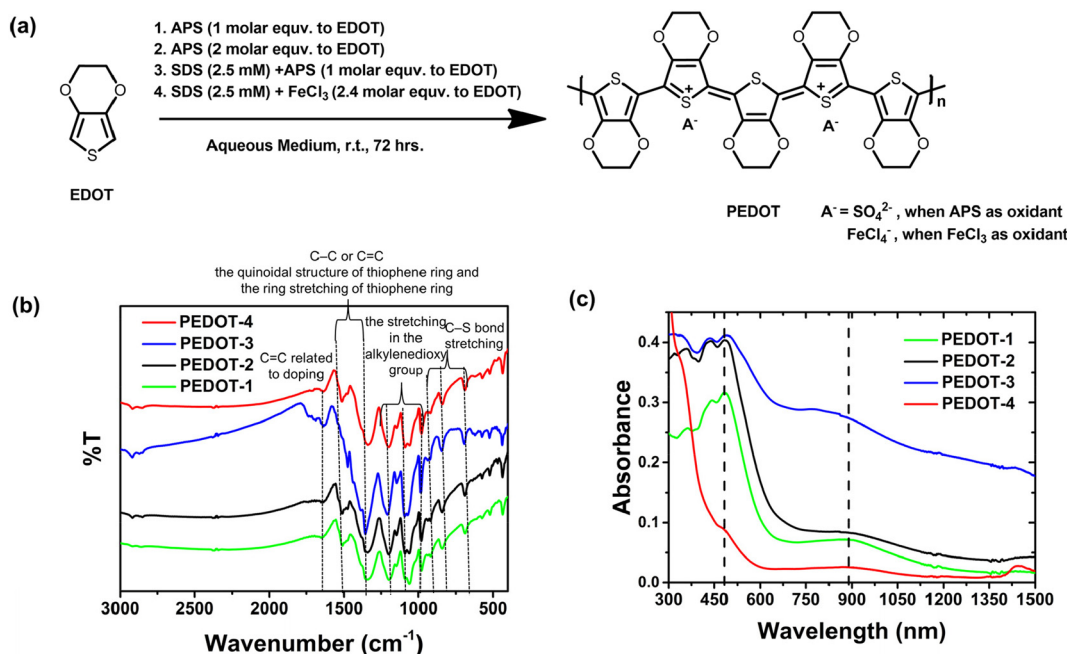
Fig. 1 (a) Synthetic route to PEDOT-nanomaterials, (b) FT-IR of the synthesized PEDOT nanopowders, and (c) UV-Vis-NIR absorption spectroscopy of the dispersed PEDOT in DMSO.

PEDOTs was difficult due to the insolubility or partial solubility of the PEDOT nanomaterials in organic or water media.

2.1.2 Morphologies of the chemically synthesized PEDOT nanomaterials. The intrinsic electrical and optical properties, morphology, and crystallinity of chemically synthesized PEDOTs depend on the synthetic condition (*e.g.*, reaction temperature, reaction time, types of oxidants, concentration, reaction medium, presence or absence of the surfactant in the reaction medium). Therefore, to obtain PEDOT nanomaterials with different morphologies and properties, two different oxidants with different concentrations were utilized in the presence or absence of the surfactant, SDS (see Fig. 1a and Table S2†). The morphology of PEDOT-1 and PEDOT-2 was almost similar (see Fig. 2a). PEDOT-1 dominates irregular-agglomeration with an average particle size of 132 nm, while PEDOT-2 dominates raspberry agglomeration with comparatively lower average particle size (~114 nm). The critical micelle concentration (CMC) of SDS in an aqueous medium was around 8.3 mM, which can be reduced in the presence of salt or additives.[34] In synthesizing PEDOT-3 and PEDOT-4, SDS concentration in the aqueous medium was maintained at 2.5 mM (< the CMC level), much lower than that in the reported synthesis.[32] The addition of APS or $FeCl_3$ oxidizing agent to 2.5 mM aqueous SDS solution may form a micellar template, and the PEDOT chains can grow within that template due to the hydrophobicity of EDOT-monomer (see the possible mechanism for the obtained nanomaterials in the presence of SDS by varying oxidant in Fig. 2b). In PEDOT-3, APS was used as an oxidant, and PEDOT was grown as a nanosphere inside the SDS micelle template.[26] The accumulation of nanospheres results in plum or lump-shaped morphology with

varying diameters of about 400–600 nm. In PEDOT-4, $FeCl_3$ was used as an oxidizing agent, and PEDOT was grown as a nanofiber (here, an average diameter of ~77 nm) inside the SDS micelle templates.[22,26,32] The stacking of 1D nanofibers results in a relatively ordered petal-like morphology (see Fig. 2b).

The N_2 adsorption/desorption isotherm and detailed N_2 adsorption parameters used to derive the Brunauer–Emmett–Teller (BET) surface area for different as-prepared dry PEDOT nanomaterials are shown in Fig. 3 and Table S3,† respectively. The pore size distribution was determined using NLDFT (nonlocal density functional theory) adsorption models for carbon slit-shaped pores, as shown in the inset of Fig. 3.

PEDOT-1, PEDOT-2, PEDOT-3, and PEDOT-4 exhibit BET surface areas of 21.35 m^2 g^{-1}, 30.72 m^2 g^{-1}, 11.87 m^2 g^{-1}, and 13.50 m^2 g^{-1}, respectively. The pore size distribution analysis reveals that the pores range from microporous (<2 nm) to macroporous (>50 nm), covering a broad spectrum of pore widths. Since PEDOT-1 and PEDOT-2 have 0D structures (see Fig. 2), they inherently possess large BET surface areas. PEDOT-2 has the highest BET surface area, which is due to its comparatively smaller particle size than PEDOT-1. On the other hand, the use of a surfactant in the synthesis of PEDOT-3 significantly reduced the BET surface area. This reduction is because of the aggregation and accumulation of nanospheres, forming larger, plum-shaped particles. The BET surface area for PEDOT-4 was slightly higher than that of PEDOT-3 because the change of the oxidant in the presence of a surfactant resulted in a flower-petal-shaped morphology composed of stacked 1D nanofibers with nanosized diameters. Although the BET surface area of PEDOT-4 was lower than that

(a)
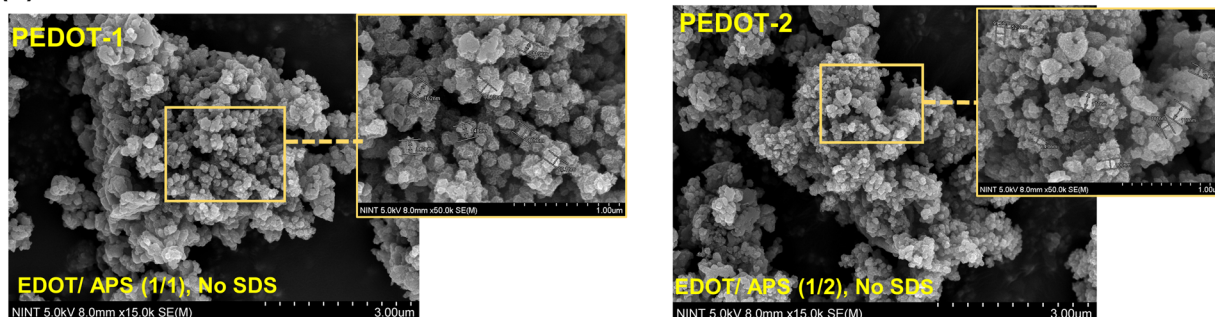
(b)
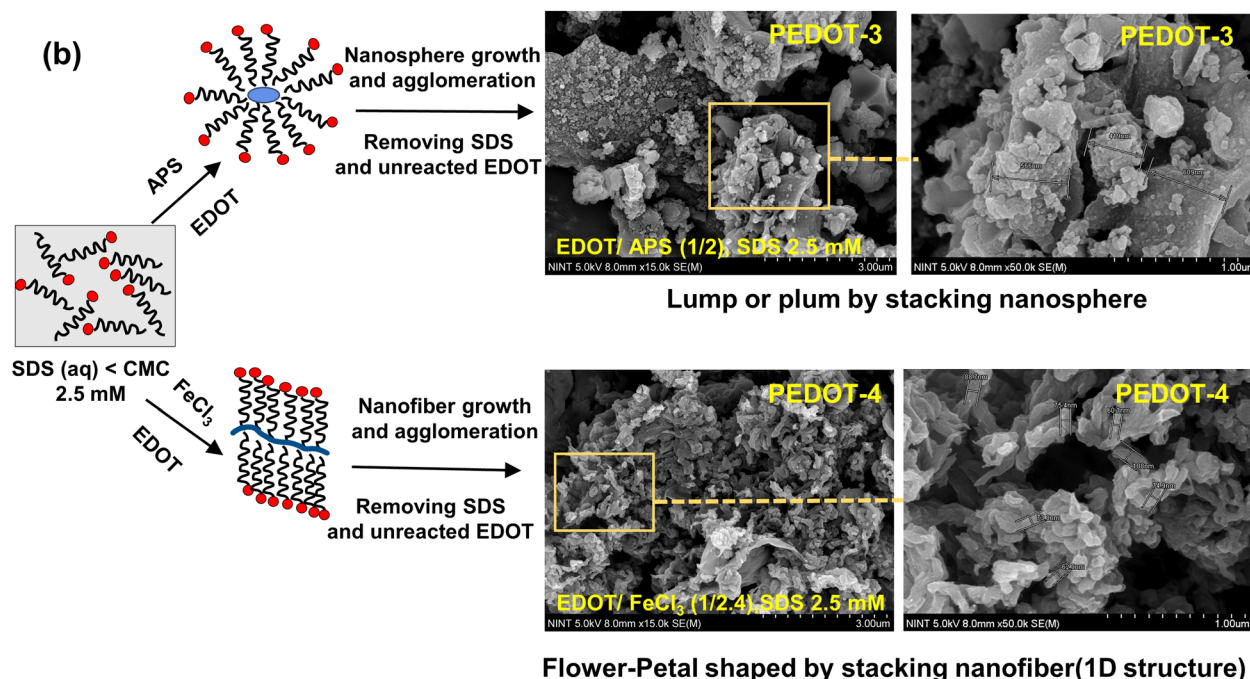
Fig. 2 (a) SEM images of the chemically synthesized PEDOTs using the APS oxidant with varying EDOT to APS concentrations. (b) Morphology of PEDOT-3 and PEDOT-4 synthesized using the APS and FeCl₃ oxidant, respectively, in the presence of 2.5 mM SDS surfactant.

of the 0D PEDOT-1 and PEDOT-2 due to the 1D nature and aggregation of nanofibers in PEDOT-4, it may still provide an extensive surface area. This is because the extended nature of the 1D nanofibers and their reduced aggregation in dispersed solutions offer advantages over 0D PEDOT-1 and PEDOT-2.

2.1.3 Crystallinity, electrical conductivity, and thermal stability of chemically synthesized PEDOT-nanomaterials. The crystal structure of PEDOTs can vary depending on the size of the counter anion and the doping level (see the XRD pattern in Fig. 4a). The diffraction peaks at $2\theta = 6.6°$, $12.7°$, and $26.8°$ can be attributed to (100), (200), and (020) reflections, respectively.[25] The diffraction peak intensity at $2\theta = 6.6°$, representing the distance between the main chain and the chain (lattice parameter a), decreases upon decreasing the dopant level. The diffraction peak at around $2\theta = 26°$, representing the interchain planar ring-stacking distance (lattice parameter b), goes

to a lower angle upon decreasing the doping level.[25,26,35] Upon increasing the doubling the APS oxidant concentration, the yield of PEDOT was increased from 66% to 80% (see the synthetic condition and yield of PEDOT-1 and PEDOT-2 shown in Table S2†); however, as confirmed by elemental analysis (see Table S1†) and the XRD pattern (see Fig. 4a), the doping level rather decreased slightly from 0.10 in PEDOT-1 to 0.079 in PEDOT-2. It is noted that no additional doping was performed, and the synthesized PEDOTs were washed several times with water and the acetone/methanol mixture. The reason for the decreased doping level with increasing APS concentration may be washing some counter anions in the purification procedure or a faster reaction rate in the presence of high APS, which may decrease the doped counter anions in the resulting PEDOT chain. The degree of amorphousness in PEDOT-2 was found to be greater than that in PEDOT-1. This was confirmed
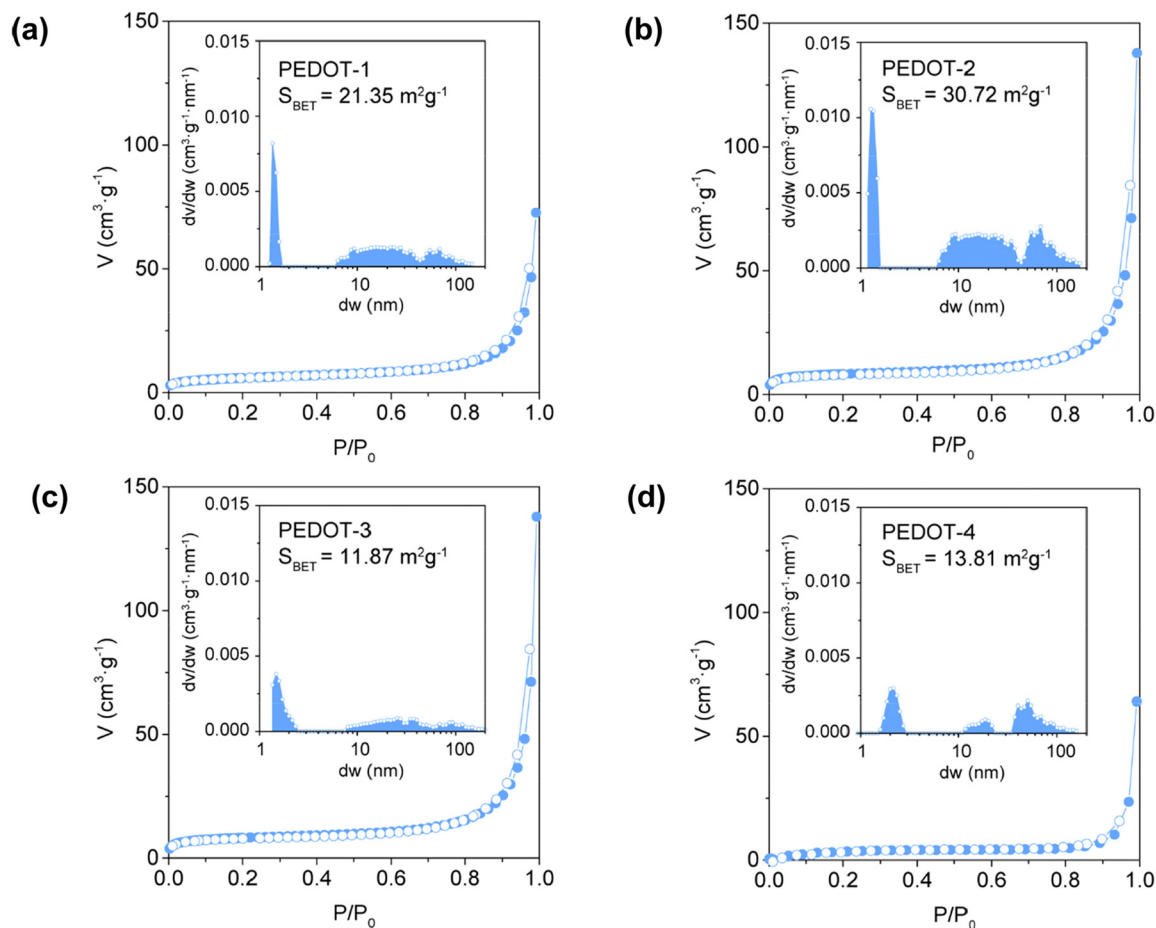
Fig. 3 N$_2$ adsorption/desorption isotherms with inset figures representing pore size distribution based on N$_2$ adsorption branch using NLDFT models for carbon slit-shaped pores of (a) PEDOT-1, (b) PEDOT-2, (c) PEDOT-3, and (d) PEDOT-4.

by observing less distinct peaks in the XRD pattern for PEDOT-2 (see Fig. 4a). The increased amorphousness can be attributed to two main factors: a lower doping level and aggregation of the nanoparticles. The synthesized PEDOT-3 was less crystalline, almost undoped, or low-doped, as confirmed by elemental analysis and the XRD pattern (see Fig. 4a and Table S1†). The negligible diffraction peak at $2\theta = 6.6°$ and the shift of the diffraction peak at $2\theta = 26°$ to a lower angle ensures the minor doping level of PEDOT-3 (see Fig. 4a). PEDOT-4 was comparatively ordered. The ordered structure of PEDOT-4 can be correlated with its high doping level by counter anions present in the reaction medium (see $2\theta = 6.6°$ and $26°$ peaks in the XRD pattern, Fig. 4a). Some sharp peaks ($2\theta = 35$–$55°$) were only noticed in the XRD pattern of PEDOT-4, which are probably due to the presence of the FeCl$_4^-$ dopant in PEDOT-4. It is consistent with TGA analysis of PEDOT-4 (see Fig. S2†). In the TGA curve, there was a noticeable amount of residue for the PEDOT-4 sample even after heating to 600 °C under an air-oxidizer (see Fig. S2†) which is because of Fe in FeCl$_4^-$.

The intrinsic electrical conductivity of the chemically synthesized PEDOTs depends on the extent of doping, mor-

phology, and nanoparticle size. The trend of intrinsic electrical conductivity of chemically synthesized PEDOTs at room temperature is shown in Fig. 4b. The highest electrical conductivity ($\sim$16.4 S cm^{-1}) was found for PEDOT-4. The high electrical conductivity of PEDOT-4 correlates with its as-synthesized high doping level (confirmed from the XRD pattern, Fig. 4a) and 1D-structural morphology (see Fig. 2b), which are suitable for electron transfer. The negligible electrical conductivity of PEDOT-3 was due to its low-doped or undoped state, confirmed by XRD patterns and elemental analysis. The moderate electrical conductivity found for chemically synthesized PEDOT-1 and PEDOT-2 by APS oxidant can be correlated to their doping level (see Fig. 4b and Table S1†) and particle size (see Fig. 2a and Table S2†). All chemically synthesized PEDOT nanomaterials were thermally stable up to 200 °C in an air-oxidizing atmosphere (see TGA curves in Fig. S2†).

2.2 Morphology and electrochemical characterization of the PEDOT counter electrode

The morphology, particle size, and electrical conductivity of PEDOT are essential factors in controlling its electrocatalytic performance. PEDOT-1 and PEDOT-2 have similar particle
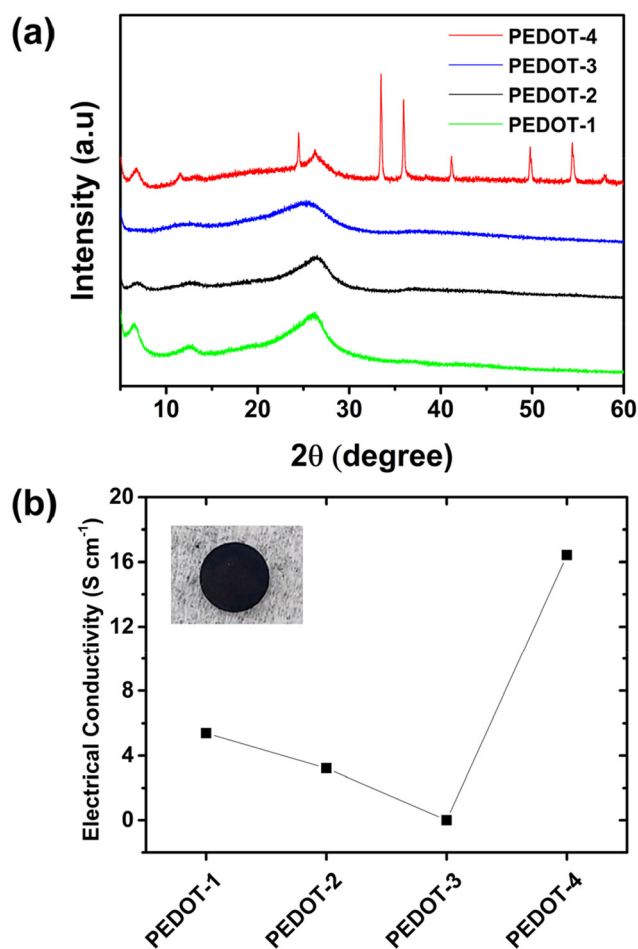
Fig. 4 The comparison of (a) XRD-patterns, and (b) intrinsic electrical conductivity of four different types of PEDOTs.

sizes, morphologies, BET surface area, and electrical conductivities. Therefore, to compare different PEDOTs, three types of PEDOT nanomaterials (PEDOT-2, PEDOT-3, and PEDOT-4) were utilized to fabricate the counter electrode. These three PEDOTs have different particle sizes, different electrical conductivities, and different morphologies. The chemically synthesized PEDOTs can be well dispersed in DMSO, DMF, or NMP. Typically, DMSO/methanol or methanol was used to disperse PEDOT nanomaterials for spin coating.[21,22] Here, the single solvent DMSO was used to disperse chemically synthesized PEDOT nanomaterials for spin coating due to its non-toxicity, polarity, and high donor number. The spin-coated PEDOT on the FTO substrate was then used as a counter electrode to fabricate symmetrical dummy cells and dye-sensitized solar cells. First, the morphology of the spin-coated PEDOT film on the FTO substrate was checked by FE-SEM (see Fig. 5). SEM analysis of the prepared counter electrode was performed directly without any thin Pt-conductive layer.

In the PEDOT-2 counter electrode, the aggregated nano-sized particles were randomly distributed on the FTO substrate with some pores. A dense PEDOT layer was formed on the FTO substrate in the PEDOT-3 counter electrode. The obtained SEM image of the PEDOT-3 counter electrode was vague due to the low intrinsic electrical conductivity of the PEDOT-3 nano-material. In the case of the PEDOT-4 counter electrode, a flower-petal-shaped film was formed by nano-sized PEDOT fibers with some pores on an FTO substrate (see Fig. 5). The high conductivity and large surface area can be suitable for increasing the catalytic activity and electron transfer to the electrode/electrolyte interface. The PEDOT-4 counter electrode, which features a continuous flower-petal shape with a high surface area due to its extended 1D nanofiber structure, can be a suitable and efficient counter electrode. It is noted that in our optimized system utilizing spin-coating with DMSO solvent, the PEDOT nanomaterials can be randomly distributed on the FTO substrate while retaining their bulk morphology. However, due to this random distribution, the thickness is not uniform across the substrate. Analysis of the cross-sectional SEM image of our best PEDOT-4 counter electrode reveals variations in thickness ranging from nanometers to micrometers. The maximum thickness was 2.47 μm (see Fig. 5).

The electrochemical impedance (EIS) and liner scan voltammetry (LSV) measurement of the symmetrical dummy cell by various PEDOT-counter electrodes using cobalt electrolytes were performed to determine the charge transfer resistance in the electrode/electrolyte interface, diffusion of the redox species, and electrocatalytic performance. At first, Nyquist plots of the three PEDOT-counter electrodes were compared, as shown in Fig. 6a. Usually two semicircles should be obtained in Nyquist plots of the symmetrical dummy cells; the first semicircle represents the charge transfer resistance (R_{ct}) at the electrode/electrolyte interface, and the second semicircle is related to the diffusion resistance of electrolytes redox species. In the case of PEDOT-2 and PEDOT-3, three semicircles were obtained, the first small semicircle in the high-frequency region in PEDOT-2 and PEDOT-3 is likely attributed to the transmission resistance of the electron (R_{tm}) on the PEDOT surface while second semicircle represent R_{ct} at the PEDOT electrode/electrolyte interface.[36] The additional semicircle in the high-frequency region due to the probable electron transmission resistance can be attributed to the discontinuous morphology of the PEDOT-2 counter electrode, despite the moderate intrinsic electrical conductivity of PEDOT-2. In the case of PEDOT-3, this probable electron transmission resistance (first small semicircle) can be attributed to the very poor intrinsic electrical conductivity of PEDOT-3 and the dense morphology of the PEDOT-3 counter electrode. However, there was no such electron transport resistance observed in the PEDOT-4 counter electrode. This can be attributed to its continuous morphology, achieved through stacked 1D nanofibers, and the high intrinsic electrical conductivity of PEDOT-4.

The wide 2nd semicircles of PEDOT-3 represent its extremely high R_{ct} in the electrode/electrolyte interface compared with the R_{ct} of the other two PEDOTs. The high R_{ct} in the electrode/electrolyte interface of PEDOT-3 can be correlated to its film morphology (dense layer) and very low intrinsic electrical
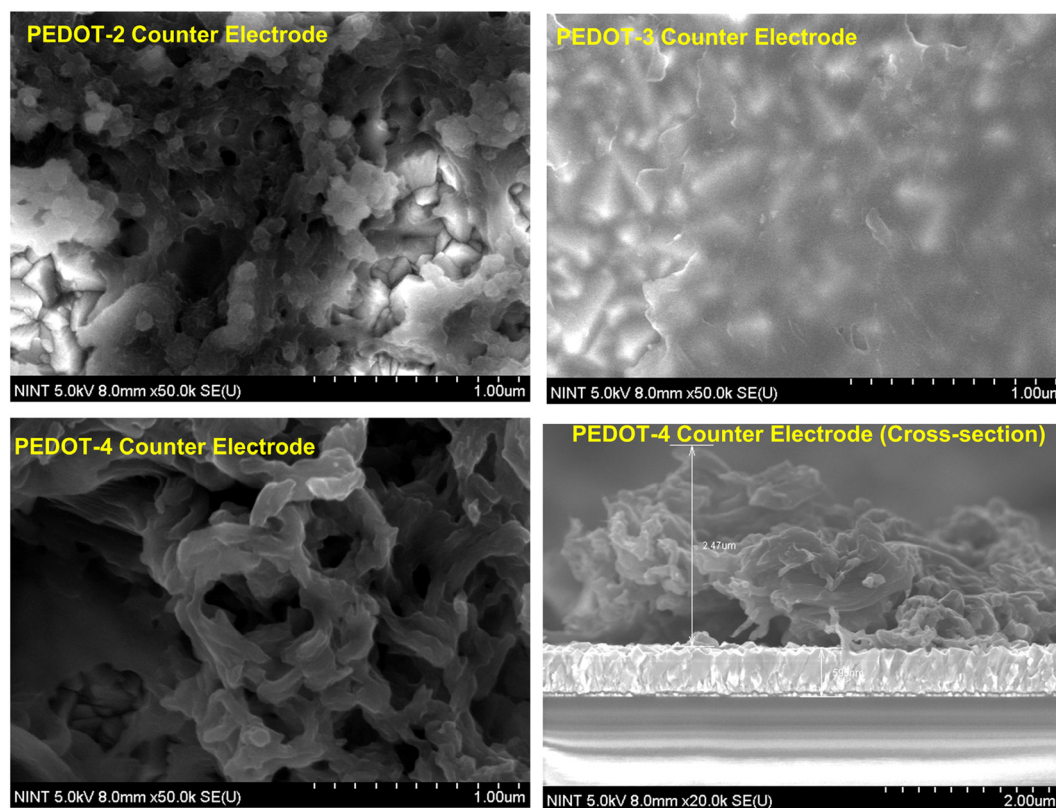
Fig. 5 FE-SEM images of the three different PEDOT–counter electrodes.
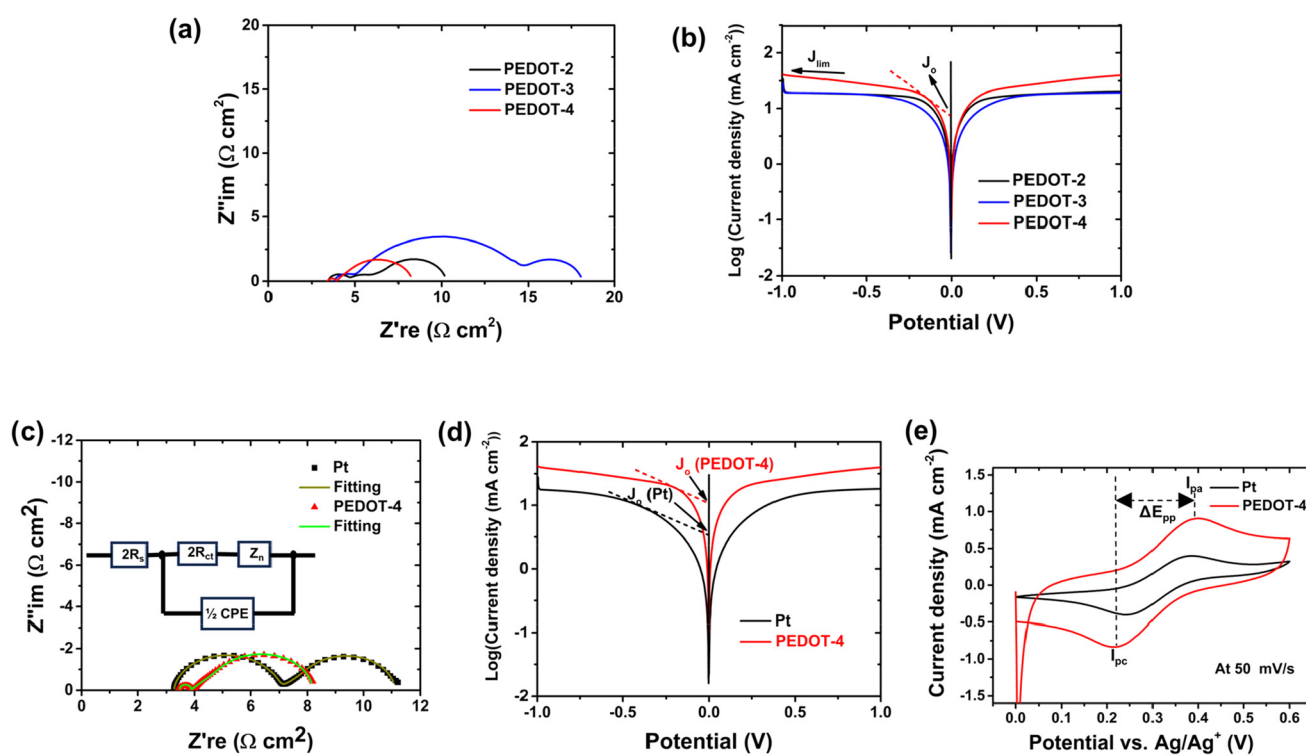

Fig. 6 Comparing (a) Nyquist plots and (b) Tafel plots of three different counter electrodes. Comparing (c) Nyquist plots, (d) Tafel plots, and (e) cyclic voltammograms of the best PEDOT–counter electrode with the Pt–counter electrode.

conductivity, which is unsuitable for fast electron transfer to catalyze the cobalt(III) reduction. The R_{ct} value in the electrode/electrolyte interface decreases in the following order: PEDOT-3 > PEDOT-2 > PEDOT-4. The R_{ct} value in the electrode/electrolyte interface depends on the morphology, surface area, and intrinsic electrical conductivity. The ordered 1D-structure of PEDOT-4 with intrinsic electrical conductivity of about 16 S cm^{-1} can efficiently transfer charge to Co^{3+} redox species. The Tafel polarization curves of the symmetrical cells using various PEDOTs counter electrodes were compared, as shown in Fig. 6b. The Tafel curve consists of three zones: polarization zone (curve at low potential, usually <120 mV), Tafel zone (curve at middle potential) and limiting diffusion zone (curve at high potential).[37] The exchange current density (J_o) and limiting current density (J_{lim}) are two important parameters that can be obtained from the Tafel polarization curves to describe the electrocatalytic performance. The J_o value can be obtained by extending the tangent line to the zero voltage from the Tafel zone. The current density of the intersection of the cathodic branch and the equilibrium potential line can be described as J_o. The J_o value is inversely correlated with change transfer resistance; therefore, the higher J_o value indicates higher catalytic ability.[37,38] The J_{lim} can be obtained by extending the tangent line from the diffusion zone and the intersection of the cathodic branch with the Y-axis regarded as J_{lim} (see Fig. 6b). J_{lim} is directly correlated with the diffusion of the redox species. The higher J_{lim} indicates faster diffusion of redox species in the electrode.[39] Among the three types of

PEDOT electrodes, PEDOT-4 exhibits the highest J_o and J_{lim}, while PEDOT-3 exhibits the lowest J_o and J_{lim}. Therefore, the catalytic ability of different PEDOT counter electrodes is in the following order: PEDOT-4 > PEDOT-2 > PEDOT-3. The Nyquist plot and Tafel polarization curve of the best PEDOT-4 counter electrode and Pt-electrodes were compared, as shown in Fig. 6c and d. The significant reduction of R_{ct} and remarkable increment of J_o and J_{lim} for PEDOT-4 compared with Pt (see Fig. 6c and d) indicate the superior electrocatalytic ability of PEDOT-4 over Pt toward Co^{3+} reduction reaction.

The cyclic voltammogram (CV) of the best PEDOT counter electrode (PEDOT-4) was also compared with the CV of the Pt-counter electrode. The CV of the counter electrode was performed using a three-electrodes system, where Ag/AgCl and Pt-wire acted as a reference electrode and a counter electrode, respectively. Drop-cast Pt-or spin-coated PEDOT on the FTO substrate was used as a working electrode. The electrolytes solution for CV analysis was prepared by diluting cobalt electrolytes (100 times) with an additional 0.1 M LiClO$_3$ in acetonitrile. In the CV curve, the cathodic peak represents Co^{3+} reduction, and the anodic peak is related to Co^{2+} oxidation.

A high peak current density (I_p) correlates with the high catalytic activity of the counter electrode and lower peak-to-peak separation (ΔE_{pp}) relates to higher electrochemical rates of redox reactions.[40–42] The higher cathodic peak current density ($I_{pc, PEDOT-4}$ −0.84 mA cm^{-2}) than that of Pt-counter electrode ($I_{pc, Pt}$, −0.40 mA cm^{-2}) and comparable ΔE_{pp} for PEDOT-4 ($\Delta E_{pp, PEDOT-4}$ 0.18 V) with Pt ($\Delta E_{pp, pt}$ 0.14 V) at
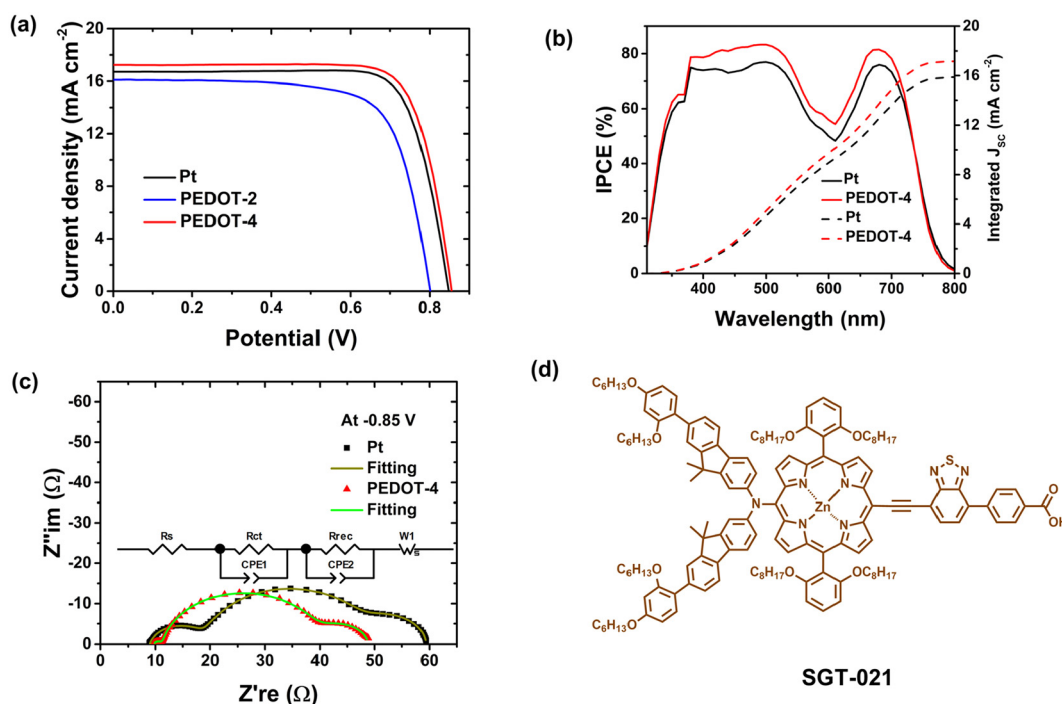

Fig. 7 (a) J–V curves, (b) IPCE with integrated current density, and (c) Nyquist plots of DSSCs using PEDOT and Pt–counter electrodes. (d) The structure of porphyrin dye used to fabricate the device.

Table 1 Photovoltaic performance of porphyrin dye, SGT-021-sensitized solar cells using various counter electrodes under simulated 1-sun (standard AM 1.5G) illuminations[a]

Device	J_{sc} (mA cm^{-2})	V_{oc} (mV)	FF (%)	PCE (%)	J_{sc}^{IPCE} (mA cm^{-2})
Pt	16.72 (16.34 ± 0.37)	848 (853 ± 5.30)	78.41 (79.54 ± 1.12)	11.11 (11.09 ± 0.03)	15.89
PEDOT-2	16.10 (15.36 ± 1.25)	801 (797 ± 6.02)	72.18 (72.76 ± 1.62)	9.31 (8.90 ± 0.61)	—
PEDOT-4	17.24 (17.17 ± 0.09)	855 (852 ± 7.67)	78.38 (78.48 ± 0.12)	11.56 (11.47 ± 0.16)	17.15

[a] The average value was reported from the results of three devices with the margin of error (95% confidence level). The device's active area was 0.3 cm^2, and the J–V measurement was performed with a black metal mask with an aperture area of 0.141 cm^2. The composition of the cobalt electrolytes was 0.22 M $[Co^{2+}(bpy)_3](TFSI)_2$, 0.05 M $[Co^{3+}(bpy)_3]$ (TFSI)$_3$, 0.1 M LiTFSI and 0.8 M TBP in acetonitrile.

50 mV s^{-1} scan rate (see Fig. 6e, Fig. S3 and Table S4†) indicate that PEDOT-4 can be the best alternative of Pt catalyst for the Co^{3+} reduction reaction.

2.3 Photovoltaic performance of dye-sensitized solar cell using spin-coated chemically synthesized PEDOT counter electrode

Based on the electrochemical parameters described in the previous section, PEDOT-2, and PEDOT-4 counter electrodes were utilized to fabricate full cells and compare with the device of Pt-electrode. Here, our developed porphyrin dye, SGT-021,[43] was used to fabricate DSSC with cobalt electrolytes and PEDOT-counter electrodes. The J–V curves under simulated 1-sun conditions are shown in Fig. 7a and summarized in Table 1.

SGT-021 dye is a promising dye for cobalt electrolytes because of its 0.28 V driving force, enabling efficient dye regeneration by cobalt(II) redox species,[44] and its broad visible light absorption (see IPCE spectrum in Fig. 7b). Using the PEDOT-4 counter electrode, excellent power conversion efficiency (PCE) of 11.6% was achieved, which was higher than that for PCE (11.1%) of the device using the Pt-counter electrode. The enhancement of PCE using PEDOT-4 counter electrode was because of significant enhancement of J_{sc} with comparable V_{oc}, which directly reflects the superior electrocatalytic ability of PEDOT-4 over Pt for Co^{3+}-reduction reaction. The enhanced J_{sc} value for the PEDOT-4 device was correlated with the IPCE spectrum with integrated J_{sc} value (see Fig. 7b).

The EIS of PEDOT-4 and Pt-devices were performed under dark conditions at −0.85 V at room temperature to compare the recombination resistance (R_{rec}) and charge transfer resistances (Fig. 7c and Table 2).

Similar R_{rec} values for these two devices indicate their comparable V_{oc}. However, lower charge transfer resistance in the counter electrode (R_{ct} (CE)) and diffusion resistance (R_w) again ensured the reason for the higher J_{sc} value for the PEDOT-4-

device (see Table 2 and Fig. 7c). Using the PEDOT-2 counter electrode, the PCE was relatively low because of low J_{sc}, V_{oc}, and FF, which indicated its poor catalytic ability for Co^{3+} reduction. It is noted that to obtain high photovoltaic performance, optimization of the counter electrodes is also quite an important factor. Here, excellent PCE was obtained due to the fabrication of the device using the optimized counter electrode. The use of DMSO solvent in spin-coating plays a crucial role in retaining the surface morphology of the 1D-structure for PEDOT-4, suitable to catalyze the Co^{3+} reduction by fast transferring electrons to the redox species of the electrolytes. PEDOT nanomaterials synthesized here are stable (see our TGA data in Fig. S2†), indicating stability in the range of 200–300 °C under an air-oxidizer atmosphere. The initial stability test of the DSSC using a PEDOT-counter electrode was tested under ambient conditions. After 200 hours, no significant loss of photovoltaic performance was found (see the comparison of J–V curves of the fresh and aged cell in Fig. S4†). Here, the counter electrode was developed by chemically synthesized PEDOT, which is cheap and scalable, and fabricated by a simple spin-coating process with the green solvent, DMSO. The drying temperature of this counter electrode was 70 °C in a vacuum oven. Therefore, this PEDOT counter electrode can be fabricated on a flexible substrate to form a flexible DSSC. The developed counter electrode by chemically synthesized PEDOT can compete with the traditional Pt counter electrodes and be an effective alternative to expensive Pt-counter electrodes.

3. Conclusions

Chemically synthesized PEDOTs with diverse structural morphologies and electrochemical properties were evaluated as electrocatalysts for cobalt(III) reduction. PEDOTs (PEDOT-1 and PEDOT-2) obtained by aqueous oxidative polymerization by APS have nano structural morphology with particle size around 114–130 nm and moderate intrinsic electrical conductivity (3–6 S cm^{-1}). Using the SDS surfactant below the CMC level at room temperature, the APS oxidant produces plum/lump-shaped agglomerated PEDOT (PEDOT-3). In contrast, the FeCl$_3$ oxidant produces PEDOT (PEDOT-4) with flower petal morphology stacked by 1D nanofibers having comparatively small (~70 nm) diameters. The chemically synthesized

Table 2 Resistances of SGT-021 dye-based cobalt electrolyte devices obtained by fitting the Nyquist Plots in EIS measurement under dark conditions

Device	R_s (Ω)	R_{ct} (CE) (Ω)	R_{rec} (Ω)	R_w (Ω)
Pt	8.95	9.78	27.32	13.33
PEDOT-4	9.67	1.46	27.12	10.62

PEDOT-4 exhibits maximum electrical conductivity (~16 S cm^{-1}), while PEDOT-3 gives the lowest electrical conductivity. The chemically synthesized PEDOT was deposited on the FTO substrate by spin-coating dispersed solution in green solvent DMSO. The morphology of the PEDOT-4 counter electrode has a continuous 1D structure formed by stacking nanofibers. Among three different PEDOTs, PEDOT-4 exhibits the lowest charge transfer resistance, even lower than Pt, at the electrode/electrolyte interface and better electrocatalytic ability toward Co^{3+}-reduction, characterized by EIS, LSV, and CV analysis. The better electrocatalytic ability of PEDOT-4 directly correlates to its highly ordered 1D-structure with high surface area and excellent intrinsic electrical conductivity, suitable for fast electron transfer toward Co^{3+} redox species. The electrocatalytic ability of PEDOTs directly influences the photovoltaic performance of DSSC. The outstanding PCE of 11.6% was achieved using chemically synthesized PEDOT (PEDOT-4), which has a 1D structure and excellent intrinsic electrical conductivity. The photovoltaic performance of the device using spin-coated PEDOT-4 was superior to the performance of the device using the traditional Pt-electrode because of the remarkable enhancement of current density, which is directly related to the excellent electrocatalytic and fast charge transfer ability of PEDOT-4 toward Co^{3+} redox species. Here, the developed simple and convenient fabrication of counter electrodes by chemically synthesized PEDOT-4, which is cheap and scalable, can be suitable to fabricate flexible DSSCs with cobalt, copper, or other electrolyte systems. Since PEDOT-1 and PEDOT-2 have nanostructural morphology with moderate electrical conductivity, by proper optimization, these nanomaterials also have potential in other applications.

Author contributions

Masud, Y. S. K., and H. K. K. conceived the idea and designed the experiment. Masud synthesized the materials, conducted the characterization of the materials, and fabricated and characterized the devices. M. A. conducted cyclic voltammetry and electrochemical validation. H. Z. synthesized and provided the dye. J. Y. and S. K. conducted the N$_2$ adsorption/desorption isotherms analysis for BET surface area measurement of the nanomaterials. S. S. P. validated the BET surface area and pore size distribution analysis. Masud wrote the manuscript with contributions from M. A., H. Z., J. Y., S. S. P, Y. S. K., and H. K. K., Y. S. K, and H. K. K supervised the work. All authors contributed to the review of the manuscript.

Data availability

Data for this article, including the data supporting this article, are available at Materials Data Facility at **https://doi.org/10.18126/3j2f-1h39**.

Conflicts of interest

There are no conflicts to declare.

Acknowledgements

References

1 H. Ellis, N. Vlachopoulos, L. Häggman, C. Perruchot, M. Jouini, G. Boschloo and A. Hagfeldt, *Electrochim. Acta*, 2013, **107**, 45–51.

2 E. Miglbauer, P. J. Wójcik and E. D. Głowacki, *Chem. Commun.*, 2018, **54**, 11873–11876.

3 N. Aydemir, J. Malmström and J. Travas-Sejdic, *Phys. Chem. Chem. Phys.*, 2016, **18**, 8264–8277.

4 Q. Zhou and G. Shi, *J. Am. Chem. Soc.*, 2016, **138**, 2868–2876.

5 A. Tundwal, H. Kumar, B. J. Binoj, R. Sharma, R. Kumari, A. Yadav, G. Kumar, A. Dhayal, A. Yadav, D. Singh, B. Mangla and P. Kumar, *Coord. Chem. Rev.*, 2024, **500**, 215533.

6 E. Olsen, G. Hagen and S. E. Lindquist, *Sol. Energy Mater. Sol. Cells*, 2000, **63**, 267–273.

7 H. Tian, Z. Yu, A. Hagfeldt, L. Kloo and L. Sun, *J. Am. Chem. Soc.*, 2011, **133**, 9413–9422.

8 Masud and H. K. Kim, *ACS Omega*, 2023, **8**, 6139–6163.

9 J. M. Ji, H. Zhou, Y. K. Eom, C. H. Kim and H. K. Kim, *Adv. Energy Mater.*, 2020, **10**, 1–12.

10 K. Kakiage, Y. Aoyama, T. Yano, K. Oya, J. I. Fujisawa and M. Hanaya, *Chem. Commun.*, 2015, **51**, 15894–15897.

11 Y. Ren, D. Zhang, J. Suo, Y. Cao, F. T. Eickemeyer, N. Vlachopoulos, S. M. Zakeeruddin, A. Hagfeldt and M. Grätzel, *Nature*, 2023, **613**, 60–65.

12 W. Hou, Y. Xiao, G. Han and H. Zhou, *Electrochim. Acta*, 2016, **190**, 720–728.

13 S. Lu, S. Wang, R. Han, T. Feng, L. Guo, X. Zhang, D. Liu and T. He, *J. Mater. Chem. A*, 2014, **2**, 12805–12811.

14 Q. Tang, H. Cai, S. Yuan and X. Wang, *J. Mater. Chem. A*, 2013, **1**, 317–323.

15 Y. Cao, Y. Liu, S. M. Zakeeruddin, A. Hagfeldt and M. Grätzel, *Joule*, 2018, **2**, 1108–1117.

16 A. A. Lima, G. T. Tractz, A. G. Macedo, F. Thomazi, P. R. P. Rodrigues and C. A. Dartora, *Opt. Mater.*, 2022, **132**, 112763.

17 C.-T. Li, C.-P. Lee, Y.-Y. Li, M.-H. Yeh and K.-C. Ho, *J. Mater. Chem. A*, 2013, **1**, 14888–14896.

18 L. Groenendaal, F. Jonas, D. Freitag, H. Pielartzik and J. R. Reynolds, *Adv. Mater.*, 2000, **12**, 481–494.

19 S. Nie, Z. Li, Y. Yao and Y. Jin, *Front. Chem.*, 2021, **9**, 1–8.

20 C. Li, H. Bai and G. Shi, *Chem. Soc. Rev.*, 2009, **38**, 2397–2409.

21 T. H. Lee, K. Do, Y. W. Lee, S. S. Jeon, C. Kim, J. Ko and S. S. Im, *J. Mater. Chem.*, 2012, **22**, 21624–21629.

22 N. Jeon, D. K. Hwang, Y. S. Kang, S. S. Im and D. W. Kim, *Electrochem. Commun.*, 2013, **34**, 1–4.

23 N. Paradee and A. Sirivat, *Polym. Int.*, 2014, **63**, 106–113.

24 R. Corradi and S. P. Armes, *Synth. Met.*, 1997, **84**, 453–454.

25 J. W. Choi, M. G. Han, S. Y. Kim, S. G. Oh and S. S. Im, *Synth. Met.*, 2004, **141**, 293–299.

26 W. Feng, Y. Li, J. Wu, H. Noda, A. Fujii, M. Ozaki and K. Yoshino, *J. Phys.: Condens. Matter*, 2007, **19**, 186220.

27 D. A. House, *Chem. Rev.*, 1962, **62**, 185–203.

28 W. W. Chiu, J. Travaš-Sejdić, R. P. Cooney and G. A. Bowmaker, *Synth. Met.*, 2005, **155**, 80–88.

29 Y. Wang, K. Cai and X. Yao, *ACS Appl. Mater. Interfaces*, 2011, **3**, 1163–1166.

30 O. Fichet, F. Tran-Van, D. Teyssie and C. Chevrot, *Thin Solid Films*, 2002, **411**, 280–288.

31 J. Jang, M. Chang and H. Yoon, *Adv. Mater.*, 2005, **17**, 1616–1620.

32 M. G. Han and S. H. Foulger, *Small*, 2006, **2**, 1164–1169.

33 T. Bahry, Z. Cui, A. Deniset-Besseau, M. Gervais, C. Sollogoub, T.-T. Bui and S. Remita, *New J. Chem.*, 2018, **42**, 8704–8716.

34 Y. Rharbi and M. A. Winnik, *J. Am. Chem. Soc.*, 2002, **124**, 2082–2083.

35 T. Kawai, M. Nakazono and K. Yoshino, *J. Mater. Chem.*, 1992, **2**, 903–906.

36 M. Aftabuzzaman, M. S. Ahmed, K. Matyjaszewski and H. K. Kim, *Chem. Eng. J.*, 2022, **446**, 137249.

37 S. Yun, M. Wu, Y. Wang, J. Shi, X. Lin, A. Hagfeldt and T. Ma, *ChemSusChem*, 2013, **6**, 411–416.

38 R. Kumar, V. Sahajwalla and P. Bhargava, *Nanoscale Adv.*, 2019, **1**, 3192–3199.

39 M. Aftabuzzaman, C. K. Kim, H. Zhou and H. K. Kim, *Nanoscale*, 2020, **12**, 1602–1616.

40 J. D. Roy-Mayhew, D. J. Bozym, C. Punckt and I. A. Aksay, *ACS Nano*, 2010, **4**, 6203–6211.

41 F. Gong, H. Wang, X. Xu, G. Zhou and Z.-S. Wang, *J. Am. Chem. Soc.*, 2012, **134**, 10953–10958.

42 J.-M. Ji, C. K. Kim and H. K. Kim, *Dalton Trans.*, 2021, **50**, 9399–9409.

43 S. H. Kang, M. J. Jeong, Y. K. Eom, I. T. Choi, S. M. Kwon, Y. Yoo, J. Kim, J. Kwon, J. H. Park and H. K. Kim, *Adv. Energy Mater.*, 2017, **7**, 1602117.

44 Masud, H. Zhou and H. K. Kim, *Mater. Today Energy*, 2023, **34**, 101299.